International Journal of Nanoelectronics and Materials
IJNeaM
ISSN 1985-5761 | E-ISSN 2232-1535

Characterization and properties of NiO-ZnO nanocrystalline thin films on glass substrates deposited by SILAR technique

Sandeep Kumar Soni [a] *, R. S. Singh [a], and Pankaj Soni [b]

[a]*Department of Physics, Government V.Y.T. PG Autonomous College, Durg (C.G.), India*
[b]*Department of Chemistry, Government Danveer Tularam Postgraduate College, Utai, Distt.- Durg (C.G.), India*
** Corresponding author. Tel.: +91-7566868339; e-mail: san333deep@yahoo.co.in*

Received 07 October 2024, Revised 25 December 2024, Accepted 2 January 2025

ABSTRACT

Utilizing the Successive Ionic Layer Adsorption and Reaction (SILAR) technique, nanocrystalline thin films of pure zinc oxide (ZnO), nickel oxide(NiO) and their composites in varying ratios were deposited onto glass substrates. The morphology of these films was characterized using scanning electron microscopy (SEM) and energy-dispersive X-ray Spectroscopy (EDX). X-ray diffraction (XRD) spectroscopy and Raman spectroscopy were employed for phase identification of ZnO and NiO, while Fourier transform infrared (FTIR) spectroscopy provided valuable insights into their structural and functional characteristics. UV-visible spectroscopy demonstrated that transmittance increased with higher ZnO content, while a significant decline and shift towards lower wavelengths occurred with increasing NiO levels. Photoluminescence (PL) spectroscopy revealed various defect-related emission features. Notably, an increase in ZnO content resulted in a red shift of the optical energy bandgap, ranging from 3.51 eV to 3.12 eV, alongside a decrease in electrical resistivity. These findings suggest that ZnO-NiO nanocomposites possess a tunable bandgap making them promising candidates for optoelectronic applications.

Keywords: *ZnO-NiO nanocomposite, Thin films, Optical band gap, XRD, SILAR*

1. INTRODUCTION

The unique properties of nanocrystalline thin films have garnered significant research interest due to their potential applications across various fields such as electronics, optoelectronics and energy storage. Among the diverse types of nanocrystalline thin films, nickel oxide-zinc oxide (NiO-ZnO) nanocomposites have emerged as particularly promising materials exhibiting a wide range of functionalities and improved performance. Nano-composites are characterized as materials comprising two or more phases with at least one phase having dimensions in the nanometer range. Nanocomposite thin films have been extensively studied because of their enhanced performance beyond that of their individual constituent phases [1, 2]. Nanocomposite materials are used in various applications such as the development of efficient photovoltaic devices [3, 4], UV-photo detectors [5] and gas sensors [6, 7].

The wide energy band gap and n-type semiconductor properties of ZnO make it an excellent candidate for applications in UV and blue light emission, especially in the production of high-performance lasers and diodes. In contrast, NiO stands out as a rare p-type semiconductor, notable for its impressive thermoelectric, magnetic and electrochromic properties [8]. When synthesized at the nanometer scale, the composite of these two materials exhibits enhanced properties for various new applications in material science [1].

Thin films of zinc oxide (ZnO) and nickel oxide (NiO) have been successfully produced using various deposition techniques [7, 9–17]. In this study, we employed the SILAR (Successive Ionic Layer Adsorption and Reaction) technique, a straightforward and cost-effective method for depositing NiO-ZnO composite thin films varying in NiO and ZnO blending proportions directly onto glass plates with precise control over their thickness and composition. We took into account the thermodynamic conditions for adsorption which represent a critical step in the SILAR deposition process. We accomplished layer-by-layer deposition by sequentially exposing the substrate to metal precursors and reactants, allowing for accurate control over material growth. [9, 18]. Our study investigated the spectroscopic, structural and surface characteristics of NiO-ZnO nanocomposite thin films. We found that these properties were significantly influenced by the relative proportions of NiO and ZnO. Specifically, the presence of NiO in the nanocomposite thin films decreased transparency in the UV-Vis spectral range. Additionally, the optical bandgap of the nanocomposite exhibited a red shift, decreasing from 3.51 eV to 3.12 eV as the concentration of NiO increased.

2. EXPERIMENTS

2.1. Materials

To prepare the pure ZnO and pure NiO nanocrystalline thin films, as well as their composites, we used analytical-grade

materials. Specifically, we sourced nickel nitrate hexahydrate [$Ni(NO_3)_2$].$6H_2O$] and zinc acetate dihydrate[$Zn(CH_3COO)_2$.$2H_2O$] from HiMedia Laboratories Pvt. Ltd. Aqueous ammonia (25% NH_4OH) was obtained from Pallav Chemicals and hydrogen peroxide solution was purchased from LobaChemie Pvt. Ltd. The distilled water used for film deposition was prepared in our laboratory. We utilized glass substrates measuring 75 mm × 25 mm × 1.3 mm, which were processed in India from selected optically flat sheet glass, for the deposition of the films.

2.2. Deposition of Thin Films

In this study, we deposited pure and composite thin films of NiO and ZnO on glass substrates at ambient temperature using the Successive Ionic Layer Adsorption and Reaction (SILAR) technique. The SILAR method involves a sequential process of ionic species adsorption and reaction, leading to the formation of thin-film coatings. Initially, a layer of cationic species adsorbs onto the substrate, followed by a reaction triggered by the adsorption of a different anionic species. This reaction produces an insoluble product that coats the substrate at the nanometer scale. As illustrated in Figure 1, the SILAR setup follows a series of steps to control the deposition process: 1) Immersion of the substrate in a cationic solution. 2) Rinsing in distilled water to remove excess material. 3) Immersion in an anionic solution. 4) Rinsing again with distilled water. Repeating this process allows for incremental increases in the thickness of the deposited layer, enabling precise control over the coating's

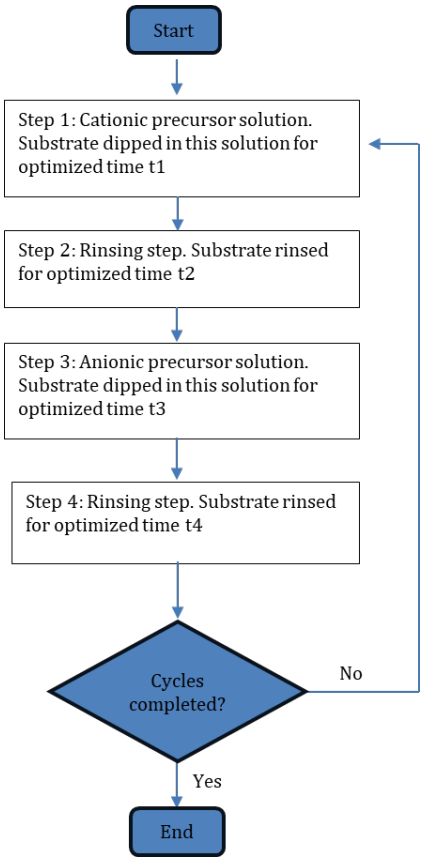

Figure 1. Flow Chart showing Successive immersion of a substrate in solutions in the SILAR method

properties. While the rinsing steps are not essential, they help remove excess material and ensure that a single ionic layer remains before the next immersion. However, rinsing can also remove adsorbed reactants or products thereby limiting growth rates. To optimize the deposition process, eliminating the intermediate rinsing step can lead to faster growth rates, but careful control is necessary to avoid uncontrolled material deposition.

To utilize the SILAR cycle, we prepared zinc acetate dihydrate [$Zn(CH_3COO)_2$.$2H_2O$] (0.8 M) and nickel nitrate hexahydrate [$Ni(NO_3)_2$].$6H_2O$ (0.8 M), along with their mixtures at different volumetric concentrations of NiO-ZnO (as shown in Table 1), using separate beakers. These solutions served as cationic precursors for the deposition of ZnO, NiO and their composite films (denoted as S2, S3, and S4) respectively. Distilled water was used as the solvent for preparing these precursor solutions. Next, we added 25% ammonia (NH_4OH)) to these solutions until white and green metal hydroxides of nickel and zinc were precipitated. Additional ammonia was introduced to dissolve these precipitates, turning the cationic precursor.

For pure ZnO into a colourless solution, while the precursors for the other compounds became deep blue. Thus Zn^{2+} and Ni^{2+} ion concentrations were optimized in these precursors for film deposition at ambient temperature. We used a temperature-controlled solution of 1% hydrogen peroxide (H_2O_2) in distilled water as an anionic precursor, maintained at temperatures between 90°C and 100°C. This solution provided hydroxide ions (OH^-) for the deposition of all films [19–21]. Before deposition, the glass substrates were treated with chromic acid and rinsed thoroughly with distilled water to remove any impurities. This cleaning process ensured optimal contact and interaction between the precursor solutions and the substrate surface.

For the deposition of pure ZnO (S1) and NiO-ZnO composite films (S2, S3 and S4), we optimized the adsorption, reaction and rinsing times after each precursor dip to 25, 30 and 5 seconds, respectively. The optimized SILAR cycle for the deposition of these films consisted of dipping substrate in their respective cationic precursor solutions for 25 seconds, intermediate rinsing in distilled water for 5 seconds, dipping in anionic precursor H_2O_2 solution for 30 seconds and a final rinsing in distilled water for 5 seconds. For pure NiO thin film (S5) deposition, we optimized the SILAR cycle to three steps eliminating intermediate rinsing (Step 2) and setting dipping times to 10 seconds. This optimized cycle consisted of a 10-second immersion in the Ni salt bath, a 10-second immersion in the H_2O_2 solution and a final 10-second rinse with distilled water. By refining the SILAR cycle parameters, we achieved precise control over the deposition process enabling the fabrication of high-quality thin films. In our experiment, we coated the glass substrate with 30 SILAR cycles. Subsequently, we annealed the samples at 300°C for 2 hours allowing a phase transformation from hydroxide to metal oxide [22]. The experimental conditions for the deposition of pure ZnO, NiO and their composite films are summarized in Table 2.

Table 1. Blending percentage of NiO-ZnO nanocomposite thin films

Films/composition in (%)	S1	S2	S3	S4	S5
NiO	0	25	50	75	100
ZnO	100	75	50	25	0

Table 2. Experimental parameters for the deposition of pure ZnO, NiO and their composite films

Films	Cationic precursor	Anionic precursor	Optimized dipping times in			
			Cationic precursor, t1 (s)	Intermediate rinsing, t2 (s)	Anionic precursor, t3 (s)	Final rinsing, t4 (s)
S1 ZnO	$Zn(CH_3COO)_2.2H_2O$ + NH_4OH	1% H_2O_2, 90–100 °C	25	5	30	5
S2 NiO:ZnO (25:75)	Mixture of $Ni(NO_3)_2].6H_2O$ and $Zn(CH_3COO)_2.2H_2O$ solutions in 25:75 ratio + NH_4OH	1% H_2O_2, 90–100 °C	25	5	30	5
S3 NiO:ZnO (50:50)	Mixture of $Ni(NO_3)_2].6H_2O$ and $Zn(CH_3COO)_2.2H_2O$ solutions in 50:50 ratio + NH_4OH	1% H_2O_2, 90–100 °C	25	5	30	5
S4 NiO:ZnO (75:25)	Mixture of $Ni(NO_3)_2].6H_2O$ and $Zn(CH_3COO)_2.2H_2O$ solutions in 75:25 ratio +NH_4OH	1% H_2O_2, 90–100 °C	25	5	30	5
S5 NiO	$Ni(NO_3)_2].6H_2O$ +NH_4OH	1% H_2O_2, 90–100 °C	10	0 (No intermediate rinsing)	10	10

2.3. Thermodynamics of Adsorption

In any spontaneous process, the net reduction in Gibbs free energy G is required (ΔG<0). This change is expressed as Equation (1):

$$dG = -SdT + VdP + \sum \mu dn + \sigma\, dA \quad (1)$$

Here, S represents entropy, T denotes temperature, P stands for pressure, μ refers to chemical potential, σ indicates surface energy, V is the volume of liquid, n signifies the number of moles and A represents the surface area of the substrate. It is important to note that adsorption leads to a decrease in surface energy.

Gibbs free energy (ΔG) is related to enthalpy described as Equation (2):

$$\Delta G = \Delta H - T\Delta S \quad (2)$$

As the entropy of the absorbed species decreases due to its confinement on the surface, so for ΔG to be negative the adsorption process must be strongly exothermic such that ΔH(<0) be dominant in the above relation.

2.4. Film characterizations

Films were characterized by various techniques. Panalytical X'pert Multifunctional Powder X-ray Diffractometer (XRD) having Cu-K_α radiation of wavelength λ = 1.5406 Å has been used for phase identification. The optical transmittance has been measured using Shimadzu Make UV-1800 Spectrophotometer in the range from 320 nm to 900 nm. The photoluminescence emission was excited at a wavelength of 325 nm using Shimadzu RF-5301 PC Spectrofluoro-photometer. Raman spectra have been recorded with an instrument named Raman: Research India. IR transmittance spectra have been taken in the range from 400 to 4000 cm^{-1} by Bruker Alpha FTIR spectrometer. EDX analysis and SEM image of the composite film have been recorded from Carl Zeiss uhr FESEM model Gemini sem 500 kmat.

3. RESULTS AND DISCUSSIONS

3.1. X-ray Diffraction Analysis

The X-ray diffraction patterns of pristine and nanocomposite films with different blending ratios of zinc oxide and nickel oxide are shown in Figure 2(a–e). For all the samples, the NiO peaks are marked by an asterisk (*) and ZnO peaks by a bold dot (•). The peaks at 31.7^0, 34.4^0, 36.2^0, 47.5^0, 56.6^0, 62.8^0 and 67.7^0 corresponding to (100), (002), (101), (102), (110), (103) and (112) respectively (JCPDS: 65-3411) points to the growth of ZnO crystals exhibiting a wurtzite hexagonal lattice. Peaks at 37.3^0, 43.3^0, 62.8^0 and 79.6^0 corresponding to (111), (200), (220) and (222) respectively (JCPDS: 73-1519) confirm the growth of the cubic phase of NiO nanoparticles. An additional peak at 75.0^0 has been seen in the S4 sample which may be due to the tetragonal nickel-zinc peak (JCPDS: 10-0209) [23]. In S3 some peaks of NiO are missing and in S4 ZnO peaks are diffused which might be due to poorly crystallized or small particle size in that particular direction [24–25].

The interplanar distances (d) in angstroms (Å) have been calculated from Bragg's law of diffraction as in Equation (3) and are summarized in Table 3.

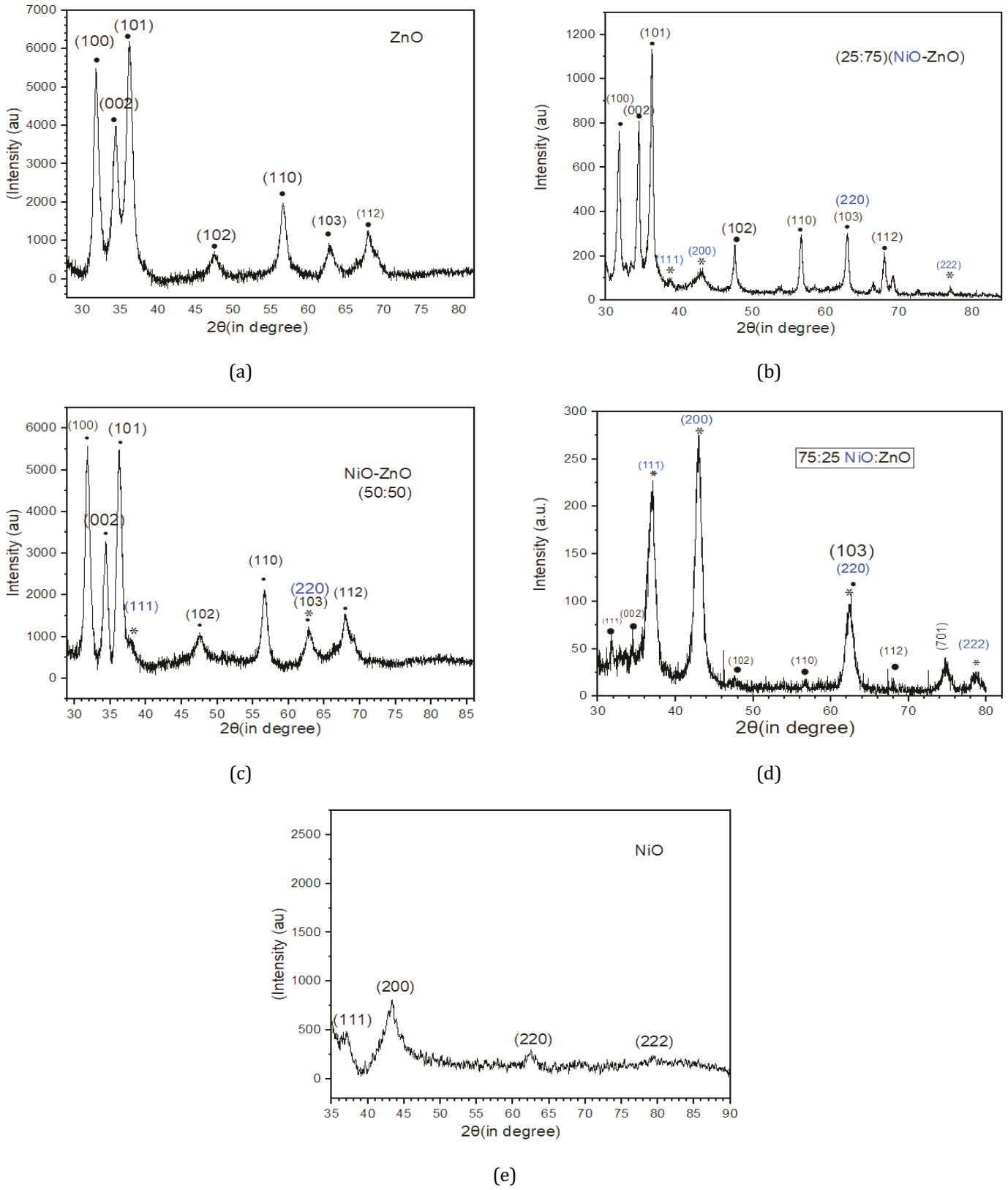

Figure 2. XRD of (a) S1pure (ZnO), (b) S2 (NiO-ZnO) (25:75), (c) S3 (NiO-ZnO) (50:50), (d) S4 (NiO-ZnO) (75:25), and (e) S5 pure (NiO)

$$2d\sin\theta = n\lambda \quad (3)$$

The average crystallite size (D) for the samples under investigation was determined using Scherrer's formula [1] as in Equation (4):

$$D = 0.94\lambda/\beta\cos(\Theta) \quad (4)$$

where D is the crystallite size in nm, λ = 1.5406 Å is the copper k_α line wavelength, β is peak broadening i.e. Full Width at Half Maxima (FWHM) in radians, θ is the diffraction angle. Calculated average crystallite sizes are summarized in Table 4 which ranged from 5.7 to 9.44 nm [26]. As the percentage of ZnO in the composite film is increased the crystallite size increases.

The dislocations in the crystal system are measured in terms of dislocation density (σ) and expressed as Equation (5) [12]:

$$\sigma = 1/D^2 \quad (5)$$

The XRD peaks inform about another very important parameter which is a measure of distortion in the material and is calculated by the Wilson formula [14] as in Equation (6).

$$\varepsilon = \beta/4\tan\theta \quad (6)$$

Calculated values of D (nm), σ (10^{16} m^{-2}) and ε (10^{-3}) from the XRD data are summarized in Table 4.

The data presented in the table indicates that the incorporation of ZnO into NiO significantly alters the properties of the films. This addition leads to a notable increase in the average crystallite size, suggesting a more organized microscopic structure. Concurrently, there is a decrease in dislocation density, indicating an improvement in crystallinity and a reduction in structural defects.

Moreover, the analysis of strain values shows a downward trend with increasing ZnO concentration, reflecting a more stable and uniform film structure, which enhances overall performance. The ability to adjust the ZnO content presents an opportunity to fine-tune the physical properties of the films. By carefully varying the ZnO ratio, one can optimize various characteristics including mechanical strength resulting in greater durability, and optical transparency allowing for improved light transmission and electrical conductivity enhancing performance in electronic applications. Therefore, the strategic incorporation of ZnO offers a versatile method for customizing these films for specific uses.

Table 3. The interplanar spacing of the nanocystalline materials of pure and composites of NiO and ZnO with varying blending ratios

Prepared thin films	(hkl)	Interplanar distance, d (Å)
S1	(100)	2.809
	(002)	2.606
	(102)	2.478
	(110)	1.623
S2	(101)	2.478
	(200)	2.089
	(203)	1.477
S3	(100)	2.809
	(002)	2.606
	(101)	2.478
	(110)	1.623
	(220)	1.480
S4	(111)	2.436
	(200)	2.105
	(103)	1.487
S5	(200)	2.089

Table 4. D (nm), σ (10^{16} m^{-2}), and ε (10^{-3}) values from the XRD data

Prepared thin films	Average crystallite size, D (nm)	Dislocation density, σ (10^{16} m^{-2})	Strain, Ɛ (× 10^{-3})
S1	9.44	1.12	11.26
S2	8.68	1.33	12.56
S3	8.58	1.36	11.58
S4	6.96	2.06	13.12
S5	5.70	3.08	16.50

3.2. UV-Visible Transmittance Spectra Analysis

The transmittance of all the films was measured at ambient temperature over the wavelength range of 320 to 900 nm, at normal incidence. The results presented in Figure 3 indicate that as the proportion of NiO in the nanocomposite films increases (from samples S2 to S4), the transmittance decreases significantly [27]. These composite films appear to be more effective at capturing light, which is beneficial for various applications in photovoltaic system design. Additionally, there is a rapid decline in light transmittance at the onset of the visible spectrum, indicating that the material begins to absorb light substantially. This absorption shifts to shorter wavelengths as the percentage of NiO increases [1].

3.3. Film Thickness Measurement

Film thickness is estimated by the following relation,

$$t = (\lambda_1 \lambda_2)/[2(n(\lambda_1)\lambda_2 - n(\lambda_2)\lambda_1)] \quad (5)$$

where λ_1 and λ_2 are the corresponding wavelengths at two consecutive maxima or minima and $n(\lambda_1)$ and $n(\lambda_2)$ are corresponding indices of refraction at these wavelengths. Here refractive index n is given by following the equation,

$$n = [N + (N^2 - n_0^2 n_1^2)^{1/2}]^{1/2} \quad (6)$$

where

$$N = [(n_0^2 + n_1^2)/2] + [2n_0n_1(T_{max} - T_{min})/(T_{max}T_{min})] \quad (7)$$

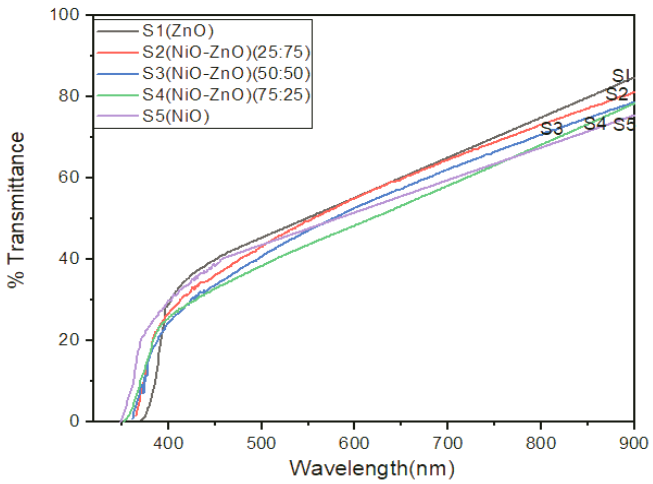

Figure 3. %Transmittance curve of pure ZnO, NiO and ZnO-NiO nanocomposites

The refractive indices of the media between which the film is formed are represented as n_0 and n_1, corresponding to the glass substrate and air, respectively [28]. Small oscillations within the transmittance curves have been employed to calculate the film thickness, estimated to be around 900 nm. For instance, in sample S3, the minor oscillatory component has been magnified in Figure 4. The refractive indices, n_{376}=1.52 and n_{374}=1.61, were determined using the expression for two consecutive maxima at wavelengths of 376 nm and 374 nm, leading to a thickness value of 976 nm from Equation (5). Other samples exhibited thickness values within the range of 975 nm to 989 nm.

3.4. Tauc's Plot and Optical Energy Band Gap

The absorption coefficient (α) in Equation (8) is obtained from transmittance (T) and the film thickness (d):

$$\alpha = [\ln(1/T)]/d \quad (8)$$

For direct allowed transitions, the absorption coefficient is linked to the optical band gap (E_g) by the Equation (9):

$$\alpha h\nu = A(h\nu - E_g)^{1/2} \quad (9)$$

where A is a constant, h is the Planck constant and ν is the frequency of incident light. The Tauc plot, which displays $(\alpha h\nu)^2$ versus hν, is presented in Figure 5 for all the films. The optical band gap values (Eg) were estimated by extrapolating the linear portion of Tauc's plot to α = 0, as shown in Table 5. The single slops indicate that the material exhibits characteristics of a direct band gap. As detailed in Table 5, it is clear that the optical band gap decreases with an increasing ZnO composition in the composite. This decrease may be due to an increase in crystallite size, as noted in Table 4 [1, 11].

Table 5. Bandgap energy values (E_g) estimated from Tauc's plot

Prepared thin films	Eg (eV)
S1	3.12
S2	3.25
S3	3.31
S4	3.36
S5	3.51

3.5. Photoluminescence (PL) Analysis

The photoluminescence (PL) emission spectra of pure and composite films of NiO and ZnO, with varying blending ratios, are presented in Figure 6. The pure NiO thin film exhibits a peak at 393 nm, which corresponds to the radiative transition of electrons from the conduction band to the valence band. Additionally, there is a broad peak at 496 nm, attributed to defects related to nickel interstitials and oxygen vacancies when excited with an ultraviolet wavelength of λext = 325 nm [29]. In comparison, the PL spectrum of the pure ZnO film shows two peaks: one at 386 nm in the UV region, which corresponds to near-band-edge emission characteristic of ZnO's wide band gap and another at 497 nm known as deep-level emission [30].

In contrast to the PL of pure ZnO and NiO films, the emission peaks in the NiO/ZnO composite films are notably diminished, accompanied by the broadening of the intrinsic emission peak. This indicates that the inclusion of NiO in the sample significantly reduces the likelihood of recombination between photo-excited electrons and holes [31], while in S2 (ZnO75/NiO25), a broad peak with less intensity around 443 nm in the range 410 nm to 450 nm in pure ZnO (S1) form shifted to the left with increased intensity. This might be ascribed to band gap renormalization caused by the formation of ionization [32–33].

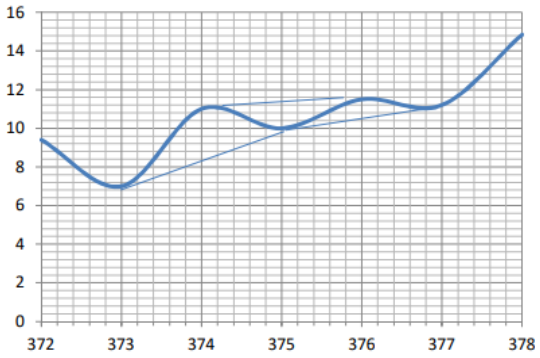

Figure 4. (Enlarged) Oscillatory part of transmittance curve (% transmittance vs wavelength in nm) of the film S3 NiO-ZnO (50:50).

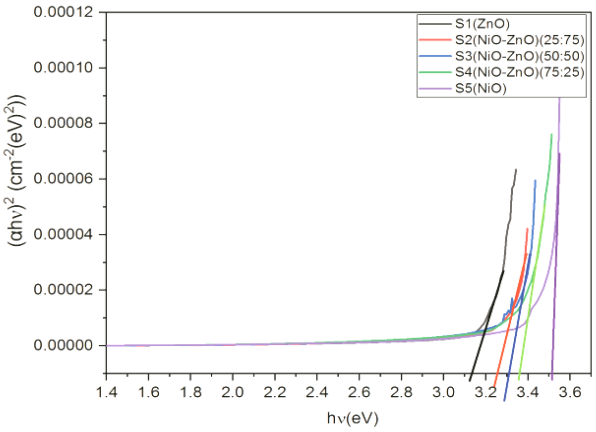

Figure 5. Tauc Plot for annealed films at 300^{0}C for 2 hrs

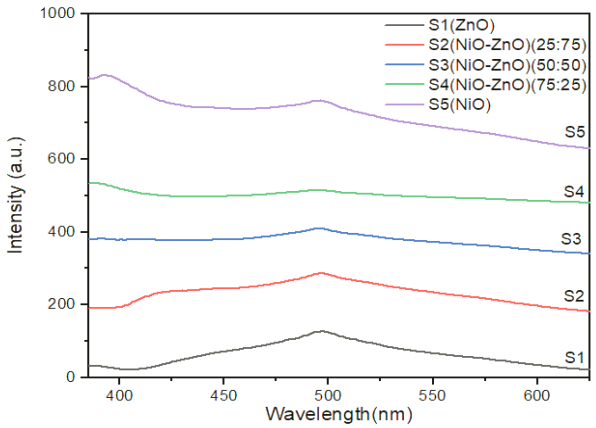

Figure 6. Photoluminescence Spectra of pure ZnO, NiO and NiO-ZnO nanocomposites

3.6. Raman Spectra Analysis

The Raman scattering spectra of pure ZnO, pure NiO and the composite film S3 are shown in Figure 7. The wurtzite structure of ZnO presents a zone-center optical phonon mode that includes A1, E1 and 2E2 modes. The A1 and E1 modes exhibit polar behaviour and separate into transverse optical (TO) and longitudinal optical (LO) branches, while the E2 mode represents a non-polar phonon mode. Spectral analysis indicates that the peak at 581 cm^{-1} corresponds to the low-frequency E2 mode, and the peaks at 381 cm^{-1} and 420 cm^{-1} are assigned to the A1 (TO) and E1 (TO) modes, respectively [34–35]. The peak at 420 cm^{-1} is characteristic of the hexagonal wurtzite phase of ZnO [1]. In contrast, the NiO phase displays peaks corresponding to LO, 2TO and 2LO modes at 517 cm^{-1}, 730 cm^{-1} and 1060 cm^{-1}, respectively [1, 20, 36]. The absence of additional vibrational modes in the nanocomposite sample S3 confirms the absence of secondary phases, consistent with XRD analysis. A slight shift in the peaks observed in sample S3 may be attributed to crystalline rearrangement [1].

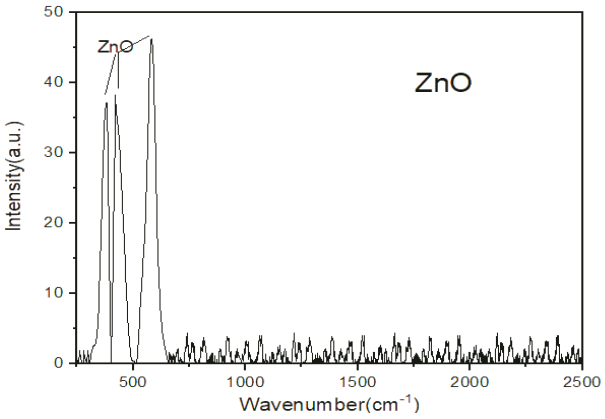

(a)

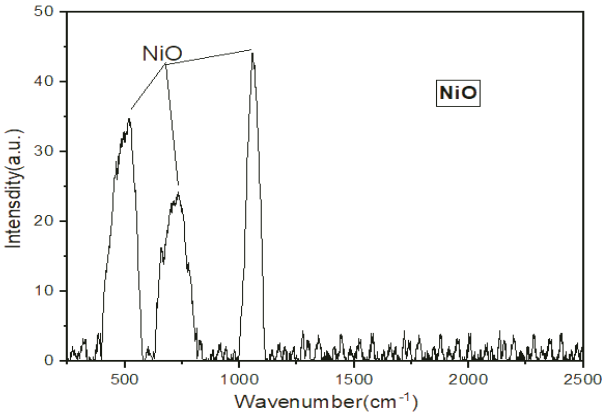

(b)

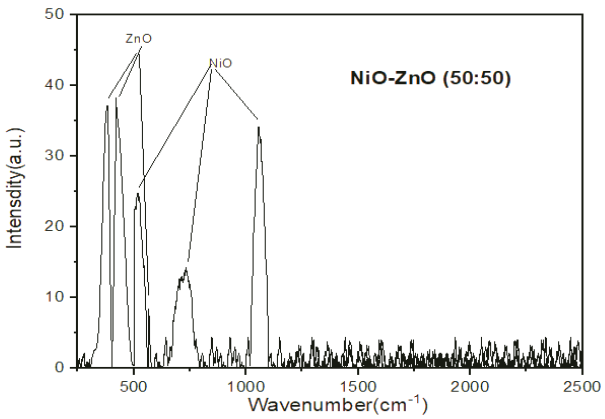

(c)

Figure 7. Raman Spectra of (a) pure ZnO, (b) pure NiO, and (c) NiO-ZnO nanocomposite (50:50)

3.7. Fourier Transforms Infrared (FTIR) Analysis

The FTIR spectra for pure NiO, and ZnO films and their composite films were recorded in the range of 400 cm^{-1} to 4000 cm^{-1}. According to the literature, peaks at 416 cm^{-1} [37–38], 427 cm^{-1} [38–39], 437 cm^{-1} [40] and 460 cm^{-1} [41] correspond to Zn–O stretching vibrations. Additionally, bond peaks at 415 cm^{-1}, 439 cm^{-1}, and 475 cm^{-1} represent Ni–O stretching vibrations [20, 42, 43]. A broad absorption peak around 3460 cm^{-1} is attributed to O–H stretching modes from adsorbed water molecules, while weak peaks between 1000 cm^{-1} and 1500 cm^{-1} are attributed to carbon impurities from leftover cationic precursors [9, 39]. As shown in Figure 8, the FTIR spectra indicate that the peaks of NiO and ZnO in the region below 600 cm^{-1} overlap, making it difficult to assign distinct peaks to each oxide phase [44].

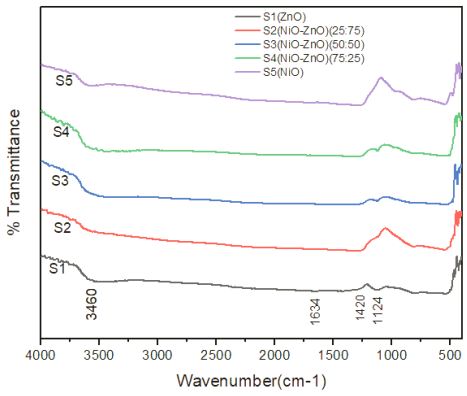

(a)

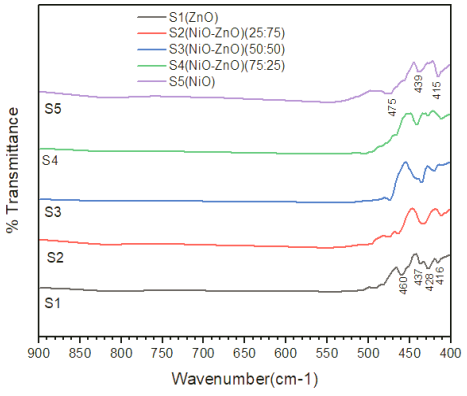

(b)

Figure 8. FTIR Spectra of pure ZnO, NiO and ZnO-NiO nanocomposite. (b) Zoomed-In FTIR Spectra of pure ZnO, NiO and ZnO-NiO nanocomposite 400–900 cm^{-1}

3.8. SEM and EDX Analysis

Scanning electron microscopy (SEM) was employed to examine the surface morphology of the NiO-ZnO (50:50) film sample, with the resulting micrograph shown in Figure 9. The image, captured at a magnification of 200 nm and a resolution of ×100000, reveals rice-like shapes [44]. Furthermore, the SEM images demonstrate a uniform distribution of particles, indicating the effective integration of NiO and ZnO within the composite material. Energy-dispersive X-ray (EDX) analysis confirmed the presence of nickel, zinc and oxygen in the nanocomposite thin film, validating its elemental composition. Figure 10 provides details on the weight and atomic percentages of these elements. The analysis indicated a Ni:Zn atomic ratio of approximately 0.84, with oxygen being the predominant element, which is consistent with the expected composition of the NiO and ZnO phases. This suggests a successful synthesis of the composite material.

3.9. Electrical Resistivity

Electrical resistivity measurements were conducted using the two-point probe technique at ambient temperature and the results are shown in Table 6. It was observed that the electrical resistivity decreases as the proportion of ZnO in the NiO-ZnO composite film increases. This decline can be primarily attributed to the increased crystallite size. Additionally, the introduction of Ni^{2+} as a donor impurity creates an energy level defect, resulting in a shallow donor level situated just below the conduction band [1].

4. CONCLUSION

This study presents the successful synthesis of both pure and composite nanocrystalline thin films of nickel oxide (NiO) and zinc oxide (ZnO) utilizing the Successive Ionic Layer Adsorption and Reaction (SILAR) technique. The research investigates the optical properties of these nanocomposites by calculating their band gaps, which were found to vary depending on the specific blending percentages of NiO and ZnO. Notably, these observed band gaps differ significantly from those of the individual metal oxides, providing strong evidence for the successful creation of innovative mixed oxide nanocomposites. Furthermore, the findings indicate that by carefully adjusting the relative proportions of NiO and ZnO in the composite films, the band gap can be strategically tailored to align with the specific requirements of various applications, thereby enhancing the potential utilization of these materials in advanced technological fields.

Optical analysis reveals that as the concentration of NiO in nanocomposite films increases, the sudden drop in transmittance shifts towards shorter wavelengths near the onset of the visible region. This shift is beneficial for various applications, such as UV detectors. Furthermore, calculations of the optical bandgap indicate that an increase in the amount of ZnO within the nanocomposite film leads to a rise in crystallite size, which results in narrower optical bandgaps. Additionally, this increase in the ZnO ratio

Table 6. Electrical resistivity of films

Sample	S1	S2	S3	S4	S5
ρ (Ω cm)	1037	1286	1500	1510	1923

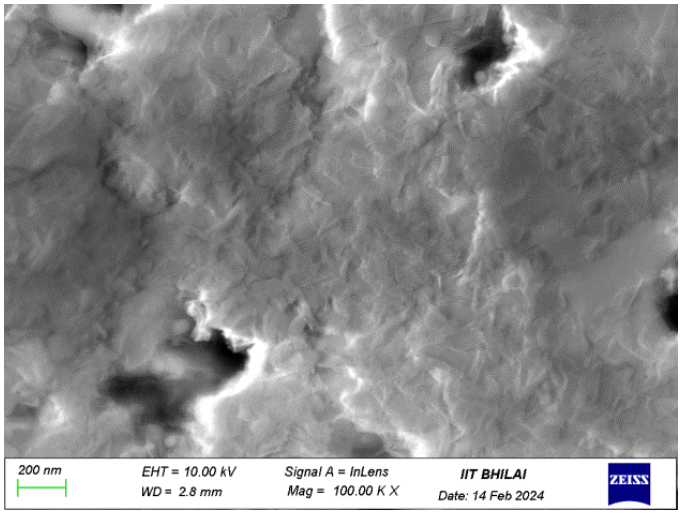

Figure 9. SEM image of Nanocomposite NiO-ZnO (50:50)

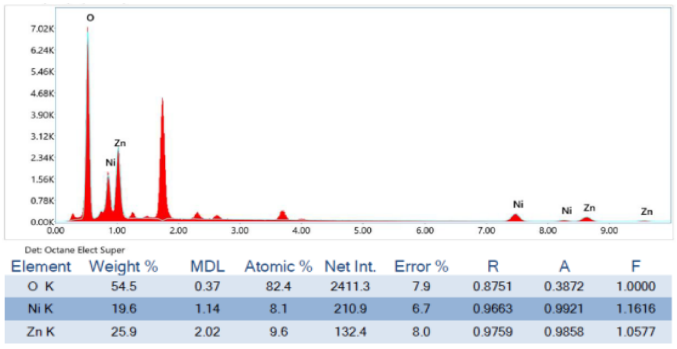

Det: Octane Elect Super

Element	Weight %	MDL	Atomic %	Net Int.	Error %	R	A	F
O K	54.5	0.37	82.4	2411.3	7.9	0.8751	0.3872	1.0000
Ni K	19.6	1.14	8.1	210.9	6.7	0.9663	0.9921	1.1616
Zn K	25.9	2.02	9.6	132.4	8.0	0.9759	0.9858	1.0577

Figure 10. EDX analysis of Nanocomposite S3 (NiO-ZnO) (50:50)

contributes to a decrease in the electrical resistivity of the nanocomposite thin films. These findings have significant implications for the optimization and design of optoelectronic devices.

REFERENCES

[1] S. Thamri, I. Sta, M. Jlassi, M. Hajji, and H. Ezzaouia, "Fabrication of ZnO-NiO nanocomposite thin films and experimental study of the effect of the NiO, ZnO concentration on its physical properties," *Materials Science in Semiconductor Processing*, vol. 71, pp. 310–320, 2017, doi: 10.1016/j.mssp.2017.08.017.

[2] A. B. Moghaddam, T. Nazari, J. Badraghi, and M. Kazemzad, "Synthesis of ZnO Nanoparticles and Electrodeposition of Polypyrrole/ZnO Nanocomposite Film," *International Journal of Electrochemical Science*, vol. 4, no. 2, pp. 247–257, 2009, doi: 10.1016/S1452-3981(23)15125-X.

[3] W.-J. Huang, S. A. de Valle, J. B. Kana Kana, K. Simmons-Potter, and B. G. Potter, "Integration of CdTe–ZnO nanocomposite thin films into photovoltaic devices," *Solar Energy Materials and*

Solar Cells, vol. 137, pp. 86–92, 2015, doi: 10.1016/j.solmat.2015.01.028.

[4] S. Bandyopadhyay, G. K. Paul, and S. K. Sen, "Study of optical properties of some sol–gel derived films of ZnO," *Solar Energy Materials and Solar Cells*, vol. 71, no. 1, pp. 103–113, 2002, doi: 10.1016/S0927-0248(01)00047-2.

[5] S. Noothongkaew, O. Thumthan, and K.-S. An, "UV-Photodetectors based on CuO/ZnO nanocomposites," *Materials Letters*, vol. 233, pp. 318–323, 2018, doi: 10.1016/j.matlet.2018.09.024.

[6] W. Shen, Y. Zhao, and C. Zhang, "The preparation of ZnO based gas-sensing thin films by ink-jet printing method," *Thin Solid Films*, vol. 483, no. 1, pp. 382–387, 2005, doi: 10.1016/j.tsf.2005.01.015.

[7] V. L. Patil, S. A. Vanalakar, P. S. Patil, and J. H. Kim, "Fabrication of nanostructured ZnO thin films based NO2 gas sensor via SILAR technique," *Sensors and Actuators B: Chemical*, vol. 239, pp. 1185–1193, 2017, doi: 10.1016/j.snb.2016.08.130.

[8] G. Vijayaprasath, P. Sakthivel, R. Murugan, T. Mahalingam, and G. Ravi, "Deposition and characterization of ZnO/NiO thin films," *AIP Conference Proceedings*, vol. 1731, no. 1, p. 080033, May 2016, doi: 10.1063/1.4947911.

[9] M. R. Das, A. Roy, S. Mpelane, A. Mukherjee, P. Mitra, and S. Das, "Influence of dipping cycle on SILAR synthesized NiO thin film for improved electrochemical performance," *Electrochimica Acta*, vol. 273, pp. 105–114, 2018, doi: 10.1016/j.electacta.2018.04.024.

[10] A. I. Inamdar, Y. Kim, S. M. Pawar, J. H. Kim, H. Im, and H. Kim, "Chemically grown, porous, nickel oxide thin-film for electrochemical supercapacitors," *Journal of Power Sources*, vol. 196, no. 4, pp. 2393–2397, 2011, doi: 10.1016/j.jpowsour.2010.09.052.

[11] A. M. Reddy, A. S. Reddy, K.-S. Lee, and P. S. Reddy, "Growth and characterization of NiO thin films prepared by dc reactive magnetron sputtering," *Solid State Sciences*, vol. 13, no. 2, pp. 314–320, 2011, doi: 10.1016/j.solidstatesciences.2010.11.019.

[12] R. S. Kate, S. A. Khalate, and R. J. Deokate, "Electrochemical properties of spray deposited nickel oxide (NiO) thin films for energy storage systems," *Journal of Analytical and Applied Pyrolysis*, vol. 125, pp. 289–295, 2017, doi: 10.1016/j.jaap.2017.03.014.

[13] Y. Akaltun and T. Çayır, "Fabrication and characterization of NiO thin films prepared by SILAR method," *Journal of Alloys and Compounds*, vol. 625, pp. 144–148, 2015, doi: 10.1016/j.jallcom.2014.10.194.

[14] B. C. Ghos *et al.*, "Influence of the Substrate, Process Conditions, and Postannealing Temperature on the Properties of ZnO Thin Films Grown by the Successive Ionic Layer Adsorption and Reaction Method," *ACS Omega*, vol. 6, no. 4, pp. 2665–2674, Feb. 2021, doi: 10.1021/acsomega.0c04837.

[15] X. Liu *et al.*, "3D hierarchically porous ZnO structures and their functionalization by Au nanoparticles for gas sensors," *Journal of Materials Chemistry*, vol. 21, no. 2, pp. 349–356, 2011, doi: 10.1039/C0JM01800G.

[16] X. Liu *et al.*, "Self-assembled hierarchical flowerlike ZnO architectures and their gas-sensing properties," *Powder Technology*, vol. 217, pp. 238–244, 2012, doi: 10.1016/j.powtec.2011.10.032.

[17] X. Liu, J. Zhang, X. Guo, S. Wu, and S. Wang, "Amino acid-assisted one-pot assembly of Au, Pt nanoparticles onto one-dimensional ZnO microrods," *Nanoscale*, vol. 2, no. 7, pp. 1178–1184, 2010, doi: 10.1039/C0NR00015A.

[18] Q. A. Adeniji, K. Odunaike, T. O. Fowodu, and A. T. Talabi, "Influence of silar cycle on the energy bandgap of iron copper sulphide (FeCuS) thin films deposited on SLG substrate," *NanoWorld Journal*, vol. 5, no. 4, pp. 49–52, 2019, doi: 10.17756/nwj.2019-072.

[19] A. C. Nwanya, P. R. Deshmukh, R. U. Osuji, M. Maaza, C. D. Lokhande, and F. I. Ezema, "Synthesis, characterization and gas-sensing properties of SILAR deposited ZnO-CdO nano-composite thin film," *Sensors and Actuators B: Chemical*, vol. 206, pp. 671–678, 2015, doi: 10.1016/j.snb.2014.09.111.

[20] A. Bouhank, Y. Bellal, and H. Serrar, "Study of thin films of nickel oxide (NiO) deposited by the spray pyrolysis method," *Journal of Chemistry and Chemical Engineering*, vol. 12, no. 3, Mar. 2018, doi: 10.17265/1934-7375/2018.03.005.

[21] T. N. Ramesh and P. V. Kamath, "Synthesis of nickel hydroxide: Effect of precipitation conditions on phase selectivity and structural disorder," *Journal of Power Sources*, vol. 156, no. 2, pp. 655–661, 2006, doi: 10.1016/j.jpowsour.2005.05.050.

[22] T. Ivanova, A. Harizanova, M. Shipochka, and P. Vitanov, "Nickel Oxide Films Deposited by Sol-Gel Method: Effect of Annealing Temperature on Structural, Optical, and Electrical Properties," *Materials*, vol. 15, no. 5, 2022, doi: 10.3390/ma15051742.

[23] D. Paul, S. Maiti, D. P. Sethi, and S. Neogi, "Bi-functional NiO-ZnO nanocomposite: Synthesis, characterization, antibacterial and photo assisted degradation study," *Advanced Powder Technology*, vol. 32, no. 1, pp. 131–143, 2021, doi: 10.1016/j.apt.2020.11.022.

[24] S. Iaiche and A. Djelloul, "ZnO/$ZnAl_2O_4$ Nanocomposite Films Studied by X-Ray Diffraction, FTIR, and X-Ray Photoelectron Spectroscopy," *Journal of Spectroscopy*, vol. 2015, no. 1, p. 836859, Jan. 2015, doi: 10.1155/2015/836859.

[25] M. O. Ansari, M. M. Khan, S. A. Ansari, J. Lee, and M. H. Cho, "Enhanced thermoelectric behaviour and visible light activity of Ag@TiO_2/polyaniline nanocomposite synthesized by biogenic-chemical route," *RSC Adv.*, vol. 4, no. 45, pp. 23713–23719, 2014, doi: 10.1039/C4RA02602K.

[26] S. Haq *et al.*, "Phytogenic Synthesis and Characterization of NiO-ZnO Nanocomposite for the Photodegradation of Brilliant Green and 4-Nitrophenol," *Journal of Chemistry*, vol. 2021, no. 1, p. 3475036, Jan. 2021, doi: 10.1155/2021/3475036.

[27] N. S. Al-Din, A. Khoudro, and A. M. Mohamad, "Structural and Optical Properties of ZnO-NiO Nanocomposite Thin Films Deposited by Spray

Pyrolysis," *International Journal of Engineering Research & Technology (IJERT)*, vol. 10, no. 10, pp. 767–773, Oct. 2021, doi: 10.17577/IJERTV10IS090046.

[28] J. C. Manifacier, J. Gasiot, and J. P. Fillard, "A Simple Method for the Determination of the Optical Constants n, k and the Thickness of a Weakly Absorbing Thin Film," *Journal of Physics E: Scientific Instruments*, vol. 9, no. 11, pp. 1002–1004, 1976.

[29] A. A. Farghali, W. M. A. El Rouby, And M. Sh. Abdel-Wahab, "Structural, Optical and Photo-catalytic Activity of Nb-doped NiO Thin Films," *Digest Journal of Nanomaterials and Biostructures* , vol. 11, no. 3, pp. 811–819, 2016.

[30] G. S. Thool, A. K. Singh, R. S. Singh, A. Gupta, and Md. A. B. H. Susan, "Facile synthesis of flat crystal ZnO thin films by solution growth method: A micro-structural investigation," *Journal of Saudi Chemical Society*, vol. 18, no. 5, pp. 712–721, 2014, doi: 10.1016/j.jscs.2014.02.005.

[31] J. Zhang and J. Li, "The Oxygen Vacancy Defect of ZnO/NiO Nanomaterials Improves Photocatalytic Performance and Ammonia Sensing Performance," *Nanomaterials*, vol. 12, no. 3, 2022, doi: 10.3390/nano12030433.

[32] A. ben Slimane *et al.*, "On the phenomenon of large photoluminescence red shift in GaN nanoparticles," *Nanoscale Research Letters*, vol. 8, no. 1, p. 342, 2013, doi: 10.1186/1556-276X-8-342.

[33] J. Long, J. Shan, Y. Zhao, Y. Ji, H. Tan, and H. Wang, "Dramatically Enhanced and Red-shifted Photoluminescence Achieved by Introducing an Electron-withdrawing Group into a Non-traditional Luminescent Small Organic Compound," *Chemistry – An Asian Journal*, vol. 16, no. 17, pp. 2426–2430, Sep. 2021, doi: 10.1002/asia.202100668.

[34] A. Khan, "Raman Spectroscopic Study of the ZnO Nanostructures," *Journal of the Pakistan Materials Society*, vol. 4, pp. 5–9, 2011.

[35] S. Rajeh, A. Mhamdi, K. Khirouni, M. Amlouk, and S. Guermazi, "Experiments on ZnO:Ni thin films with under 1% nickel content," *Optics & Laser Technology*, vol. 69, pp. 113–121, 2015, doi: 10.1016/j.optlastec.2014.12.020.

[36] J. H. Zheng, R. M. Zhang, X. G. Wang, and P. F. Yu, "Synthesizing a flower-like NiO and ZnO composite for supercapacitor applications," *Research on Chemical Intermediates*, vol. 44, no. 9, pp. 5569–5582, 2018, doi: 10.1007/s11164-018-3441-x.

[37] M. Rezaei and A. Nezamzadeh-Ejhieha, "The ZnO-NiO nano-composite: A brief characterization, kinetic and thermodynamic study and study the Arrhenius model on the sulfasalazine photodegradation," *International Journal of Hydrogen Energy*, vol. 45, no. 46, pp. 24749–24764, 2020, doi: 10.1016/j.ijhydene.2020.06.258.

[38] D. Sharma and R. Jha, "Analysis of structural, optical and magnetic properties of Fe/Co co-doped ZnO nanocrystals," *Ceramics International*, vol. 43, no. 11, pp. 8488–8496, 2017, doi: 10.1016/j.ceramint.2017.03.201.

[39] A. K. Zak, W. H. Abd. Majid, M. Darroudi, and R. Yousefi, "Synthesis and characterization of ZnO nanoparticles prepared in gelatin media," *Materials Letters*, vol. 65, no. 1, pp. 70–73, 2011, doi: 10.1016/j.matlet.2010.09.029.

[40] S. Heena Khan, S. R, B. Pathak, and M. H. Fulekar, "Photocatalytic degradation of organophosphate pesticides (Chlorpyrifos) using synthesized zinc oxide nanoparticle by membrane filtration reactor under UV irradiation," *Frontiers in nanoscience and nanotechnology*, vol. 1, no. 1, pp. 23–27, 2015, doi: 10.15761/fnn.1000105.

[41] K. Handore *et al.*, "Novel Green Route of Synthesis of ZnO Nanoparticles by Using Natural Biodegradable Polymer and Its Application as a Catalyst for Oxidation of Aldehydes," *Journal of Macromolecular Science, Part A*, vol. 51, no. 12, pp. 941–947, Dec. 2014, doi: 10.1080/10601325.2014.967078.

[42] R. Barir, B. Benhaoua, S. Benhamida, A. Rahal, T. Sahraoui, and R. Gheriani, "Effect of Precursor Concentration on Structural Optical and Electrical Properties of NiO Thin Films Prepared by Spray Pyrolysis," *Journal of Nanomaterials*, vol. 2017, no. 1, p. 5204639, Jan. 2017, doi: 10.1155/2017/5204639.

[43] F. Davar, Z. Fereshteh, and M. Salavati-Niasari, "Nanoparticles Ni and NiO: Synthesis, characterization and magnetic properties," *Journal of Alloys and Compounds*, vol. 476, no. 1, pp. 797–801, 2009, doi: 10.1016/j.jallcom.2008.09.121.

[44] A. O. Juma, E. A. A. Arbab, C. M. Muiva, L. M. Lepodise, and G. T. Mola, "Synthesis and characterization of CuO-NiO-ZnO mixed metal oxide nanocomposite," *Journal of Alloys and Compounds*, vol. 723, pp. 866–872, 2017, doi: 10.1016/j.jallcom.2017.06.288.